Received 8 August 2025; revised 26 September 2025; accepted 3 November 2025. Date of publication 6 November 2025;
date of current version 18 November 2025.

Digital Object Identifier 10.1109/OJCOMS.2025.3630072

Fundamental Limits of Target Parameter Estimation in OFDM-Based 3D NTN ISAC Systems

LUCA ARCANGELONI [1,2] (Member, IEEE), ENRICO TESTI [1,2] (Member, IEEE), LORENZO PUCCI [1,2] (Member, IEEE), AND ANDREA GIORGETTI [1,2] (Senior Member, IEEE)

[1]CNational Laboratory of Wireless Communications (WiLab), CNIT, 40126 Bologna, Italy
[2]Department of Electrical, Electronic, and Information Engineering, University of Bologna, 40126 Bologna, Italy

CORRESPONDING AUTHOR: A. GIORGETTI (e-mail: andrea.giorgetti@unibo.it)

This work was supported by the European Union under the Italian National Recovery and Resilience Plan (NRRP) of NextGenerationEU, Partnership on "Telecommunications of the Future" (Program "RESTART") under Grant PE00000001.

ABSTRACT This work investigates the fundamental performance bound of three-dimensional (3D) target localization and velocity estimation in monostatic orthogonal frequency-division multiplexing (OFDM)-based ISAC systems equipped with uniform rectangular arrays (URAs). Using the equivalent Fisher information matrix, we derive the Cramér-Rao lower bound (CRLB) for position estimation in the 3D case and show how it can be naturally reduced to existing two-dimensional bounds when the URA becomes linear, thereby generalizing prior work. Additionally, under the practical assumption of known direction of motion, particularly relevant in applications such as road traffic monitoring with unmanned aerial vehicles (UAVs), we derive a closed-form CRLB expression for the estimation of target velocity magnitude. These CRLB expressions are then used to assess the impact of key system parameters, including subcarrier count, OFDM frame size, and array geometry, on estimation accuracy. The results provide actionable insights into UAV fleet deployment strategies, such as selecting the optimal sensing node based on spatial configuration and performance metrics. Numerical simulations validate the analytical bounds and highlight fundamental trade-offs in the design of future non-terrestrial network (NTN)-based ISAC architectures.

INDEX TERMS Fisher information, Cramér-Rao lower bound, integrated sensing and communication, 3D localization, non-terrestrial networks, OFDM.

I. INTRODUCTION

INTEGRATED sensing and communication (ISAC) has emerged as a key paradigm for future sixth-generation (6G) networks by enabling the same radio infrastructure to transmit data and sense the physical environment simultaneously. This convergence underpins a wide range of future applications, including autonomous transportation, smart cities, and human-machine interfaces, all of which demand real-time tracking, situational awareness, and centimeter-level positioning accuracy [1], [2], [3]. Among the various waveform candidates for ISAC, orthogonal frequency-division multiplexing (OFDM) has gained prominence due to its inherent flexibility in the time, frequency, and spatial domains [4], [5], [6]. Already established as the cornerstone of fourth-generation (4G), fifth-generation (5G), and Wi-Fi technologies, multiple-input multiple-output (MIMO)-OFDM systems offer a robust framework for achieving both high-throughput communication and fine-grained sensing resolution [7], [8], [9]. In parallel, non-terrestrial networks (NTNs), including unmanned aerial vehicles (UAVs), high-altitude platform systems (HAPSs), and low Earth orbit (LEO) satellites, are being standardized as integral components of next-generation wireless architectures, offering flexible topology and on-demand connectivity in dynamic, remote, or emergency scenarios [10], [11]. This has led to growing interest in enabling ISAC functionalities on aerial and spaceborne platforms. In particular, UAV-enabled ISAC systems are gaining traction for their ability to operate in complex environments, enabling applications such as target localization, surveillance, and environmental monitoring [12], [13]. However, the three-dimensional (3D) mobility of these non-terrestrial platforms often introduces new challenges in parameter estimation accuracy, necessitating a deeper investigation into the fundamental limits of 3D

target position and velocity estimations. Moreover, the characteristics of NTN-based ISAC systems differ significantly from their terrestrial counterparts, leading to new modeling assumptions and operational paradigms. One prominent example is the use of UAVs for road traffic monitoring, where their elevated vantage points and wide-area coverage make them particularly suitable for sensing over large, structured environments [14], [15]. In such scenarios, targets, such as ground vehicles, often move along predefined paths (e.g., roads), making it reasonable to assume prior knowledge of their motion direction. This assumption is especially important in monostatic sensing systems, where only the radial component of the velocity can be observed. By leveraging known motion direction, it becomes feasible to infer the true velocity magnitude of the target, despite using a single sensing node. These considerations motivate the development of theoretical frameworks that incorporate such directional priors and reflect the unique geometries and constraints of aerial ISAC platforms.

Building upon the growing role of UAVs in urban and remote sensing applications, a related concept gaining traction is that of aerial highways (AHs) [16], which are predefined airspace corridors designed to support the safe and efficient navigation of drones in structured environments. Much like terrestrial highways, AHs aim to regulate UAV traffic by enforcing dedicated flight routes, particularly in dense or high-demand areas. In these structured scenarios, the assumption of known motion direction also holds for the UAVs themselves, whose trajectories are fixed by design. This prior information can be effectively exploited when UAVs act as mobile sensors or relays in monostatic ISAC configurations, enabling accurate estimation of target velocity magnitudes or supporting sensing tasks where relative motion plays a role. Together, these examples illustrate how directional priors, whether applied to sensed targets or sensing platforms, can be realistically assumed and theoretically leveraged in next-generation ISAC system design.

Understanding the fundamental performance limits of NTN-ISAC systems is essential for benchmarking algorithms and guiding system-level design choices, such as resource allocation, base station (BS) placement, and cooperation strategies [17]. As ISAC becomes a practical foundation of wireless networks, quantitatively characterizing these limits is critical to avoid inefficiencies and performance bottlenecks.

A. EXISTING WORKS

Recent studies have explored target parameter estimation in OFDM-based ISAC systems, predominantly within two-dimensional (2D) settings and often using root mean square error (RMSE) and Cramér-Rao lower bound (CRLB) as performance metrics. In [18], [19], [20], narrowband monostatic configurations are considered, where localization relies solely on angle of arrival (AoA) estimation. These works employ the CRLB to characterize fundamental trade-offs between sensing accuracy and communication performance. Similarly, [21] derives the CRLB for position estimation in a vehicular scenario under a monostatic ISAC framework, further emphasizing the role of theoretical bounds in system design. The CRLB for position and velocity estimation in cooperative monostatic and multistatic configurations within a 2D scenario employing OFDM waveforms is derived in [22].

In a different line of work, [23] investigates beamforming strategies in monostatic multi-user ISAC systems, proposing a low-complexity algorithm that jointly optimizes communication throughput and sensing precision. A single BS is considered, with co-located transmit and receive arrays, serving multiple single-antenna users while sensing a point-like target. Sensing performance is again evaluated via the CRLB.

Some recent works have addressed the fundamental limits of 3D localization, though primarily in specialized settings. In [24], the authors derive the CRLB for estimating the 3D coordinates of multiple near-field targets based on the received signal. The impact of 3D geometry is also considered in [25], where the CRLB for an OFDM waveform is computed and optimized to mitigate the angle-range coupling.

The authors of [26] study the joint estimation of range, velocity, and azimuth in OFDM-based ISAC systems equipped with a uniform linear array (ULA) in a 2D configuration. They derive CRLB expressions and propose a novel super-resolution algorithm that jointly estimates delay, Doppler, and angle by exploiting translational invariance across these domains.

In [27], the authors investigate the fundamental performance limits of extended target sensing in 3D ISAC systems. They derive the CRLBs for joint range and angular estimation (azimuth and elevation) under a monostatic radar setup, and solve two beamforming optimization problems to enable simultaneous multi-user communication and target sensing. Notably, a uniform planar array (UPA) is employed at the sensing/communication node, which aligns with the array configuration considered in our system model. However, their study does not incorporate OFDM modulation, and it does not address CRLBs for position or velocity estimation. Table 1 summarizes and categorizes all the mentioned existing works, emphasizing the key aspects.

B. OUR CONTRIBUTION

To the best of our knowledge, a unified theoretical framework that characterizes the fundamental performance limits of monostatic OFDM-based ISAC systems employing uniform rectangular arrays (URAs) in fully 3D deployments is currently lacking in the literature. This work addresses this gap by establishing a comprehensive analytical framework for target parameter estimation in such systems. In particular, we derive closed-form CRLB expressions for both target position and velocity magnitude estimation in a 3D setting,

TABLE 1. Comparison and key aspects of existing works.

Paper	OFDM	2D/3D	ULA/URA	Setup	Target	Doppler	Key aspects
[18]	✗	2D	ULA	Monostatic	Extended	✗	• Azimuth angle CRLB
[19]	✗	2D	ULA	Monostatic	Point	✗	• Azimuth angle CRLB and (x, y)-coordinates CRLB
[20]	✗	2D	ULA	Monostatic Bistatic Multistatic	Point	✗	• Azimuth angle CRLB and (x, y)-coordinates CRLB
[21]	✓	2D	ULA	Monostatic	Point	✗	• Azimuth angle CRLB • Position error bound (PEB)
[22]	✓	2D	ULA	Monostatic Bistatic Multistatic	Point	✓	• Position error bound (PEB) and velocity error bound (VEB)
[23]	✗	2D	ULA	Monostatic	Point	✗	• Azimuth angle CRLB
[24]	✗	3D	URA	Monostatic Bistatic	Point	✗	• (x, y, z)-coordinates CRLB • Near field
[25]	✓	3D	URA	Multistatic	Point	✗	• Azimuth angle, elevation angle, range CRLB
[26]	✓	2D	ULA	Monostatic	Point	✓	• Azimuth angle, range, velocity CRLB • Single antenna Tx
[27]	✗	3D	URA	Monostatic	Extended	✗	• Azimuth angle, elevation angle, range CRLB

leveraging the concept of the equivalent Fisher information matrix (EFIM).

For position estimation, the proposed framework generalizes prior results [28] by showing that the 2D case emerges naturally as a limiting instance when the array becomes effectively linear, thereby demonstrating its broad applicability.

Moreover, in realistic application scenarios where an aerial UAV localizes a ground target with a known direction of motion, we derive a closed-form expression for the CRLB associated with the estimation of the target's velocity magnitude. This assumption reflects practical use cases, such as road traffic monitoring, where targets follow constrained paths.

Finally, we demonstrate how the derived bounds can serve as critical performance metrics to guide the design and operation of UAV fleets. In particular, we demonstrate that, in specific spatial configurations, UAVs achieving tighter localization or velocity estimation bounds can be prioritized as sensing nodes, while others may be allocated to support communication tasks. This enables a dynamic and informed trade-off between situational awareness and communication coverage in ISAC-enabled aerial networks.

The main contributions of this work can be summarized as follows:

- We consider a monostatic OFDM-based 3D ISAC system equipped with URAs and derive a closed-form expression for the CRLB of target position estimation, applicable to both terrestrial and aerial targets.
- We demonstrate that the proposed 3D formulation encompasses the 2D case as a natural limiting instance when one array dimension collapses to unity, thereby generalizing and extending existing 2D models.
- We obtain a closed-form expression for the CRLB of velocity magnitude estimation under the realistic assumption that the direction of target motion is known a priori, as in road monitoring scenarios involving UAVs.
- We exploit the derived CRLB expressions to analyze the impact of key system parameters, such as the number of subcarriers, OFDM symbols, and antenna elements, on localization and velocity estimation accuracy. These insights enable informed UAV deployment strategies, including selecting the optimal sensing node from a fleet based on geometry and estimation performance. Moreover, the proposed analytical framework supports resource allocation and sensing-communication trade-offs in 3D NTN-based scenarios.

Throughout the paper, capital and lowercase boldface letters denote matrices and vectors, respectively. Additionally, $(\cdot)^{\mathsf{T}}$ and $(\cdot)^{\mathsf{H}}$ denote the transpose and conjugate transpose operator, respectively; $\|\cdot\|$ is the Euclidean norm of vectors, $\otimes$ stands for Kronecker product, and $\mathrm{diag}(a_1, \ldots, a_N)$ denotes a diagonal matrix with the elements $a_1, \ldots, a_N$ on its diagonal. We define a vector $\mathbf{a}$ as $\{a_n\}_{n=1}^{N} = [a_1, a_2, \ldots, a_N]^{\mathsf{T}}$, while $[\mathbf{X}]_{i,j}$ represents the (i, j)th element of the matrix $\mathbf{X}$. $\mathbf{I}_n$ is the $n \times n$ identity matrix, and $\mathrm{Tr}(\cdot)$ is the trace of a square matrix. $\mathbb{E}\{\cdot\}$ represents the mean value. A zero-mean circularly symmetric complex Gaussian random vector with covariance $\mathbf{\Sigma}$ is denoted by $\mathbf{x} \sim \mathcal{CN}(\mathbf{0}, \mathbf{\Sigma})$.

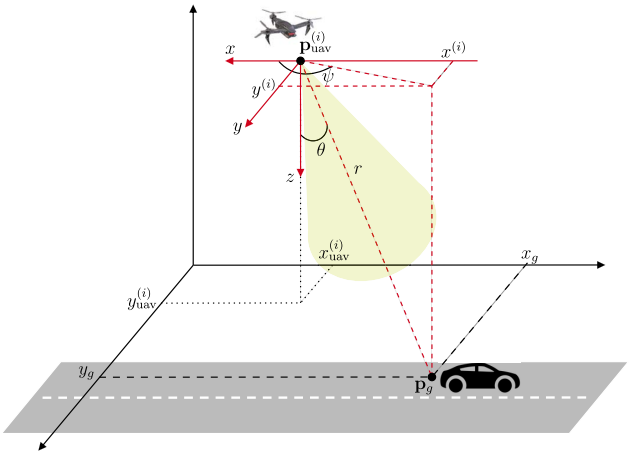

FIGURE 1. Illustrative NTN ISAC use case: a UAV localizing a ground vehicle. The local reference frame, centered at the UAV's URA, is shown in red.

The remainder of the paper is organized as follows. Section II introduces the system model for a monostatic OFDM-based ISAC architecture operating in a 3D spatial framework. In Sections III and IV, we derive closed-form expressions for the CRLBs associated with position and velocity magnitude estimation, respectively. Section V presents a method for selecting the optimal UAV from a fleet, based on the derived CRLB metrics. Section VI evaluates the estimation accuracy of target parameters through numerical simulations, leveraging the theoretical bounds established earlier. Finally, Section VII concludes the paper and outlines potential directions for future research.

II. SYSTEM MODEL

We consider a monostatic OFDM-based NTN ISAC system, as illustrated in Fig. 1. The system is equipped with a MIMO architecture with separate transmit and receive antenna arrays, enabling full-duplex operation. The transmitter simultaneously transmits communication and sensing signals, while the receiver collects radar echoes from the environment.

Both arrays are implemented as URAs, centered at the origin of the xy-plane, as shown in Fig. 2. The antenna elements are half-wavelength spaced, i.e., $d_x = d_y = \lambda/2$, where $\lambda = c/f_c$, with c denoting the speed of light and f_c the carrier frequency. Each URA comprises N_y rows with N_x antennas per row, resulting in a total of $N_a = N_x N_y$ elements.

The ISAC system transmits OFDM frames composed of K active subcarriers and M OFDM symbols, collectively referred to as the OFDM resource grid and denoted by $\mathbf{X} \in \mathbb{C}^{K\times M}$. Each element of the grid $\mathbf{X}$, denoted as $x_{k,m}$, represents a symbol drawn from a unit-power normalized complex modulation alphabet, satisfying $\mathbb{E}\{|x_{k,m}|^2\} = 1$. Subcarriers are spaced by Δf and each OFDM symbol has a total duration of $T_s = 1/\Delta f + T_{cp}$, where T_{cp} is the duration of the cyclic prefix (CP), which is used to prevent inter-symbol interference (ISI). Furthermore, the system operates under the narrowband assumption, with a total (maximum) bandwidth $B = K\Delta f \ll f_c$.

In the considered system, communication and sensing are integrated, based on the desired requirements (e.g., communication quality of service and sensing estimation accuracy), by leveraging the orthogonality of OFDM waveforms in both the time and frequency domains. This means that a portion of the frame can be used to perform sensing. Hereinafter, we indicate with K_s and M_s the total (contiguous) active subcarriers and OFDM symbols, respectively, used for sensing, and with $\mathbf{X}_s \in \mathbb{C}^{K_s\times M_s}$ a submatrix of $\mathbf{X}$ corresponding to the sensing symbol grid.

We consider a fully digital MIMO system, where precoding is applied to $\mathbf{X}_s$ to map symbols onto the transmit antennas. For each index pair (k, m), this operation produces a transmit vector $\mathbf{x}[k, m] \in \mathbb{C}^{N_a\times 1}$, given by $\mathbf{x}[k, m] = \mathbf{w}_T x_{k,m}$, where $k = 1, \ldots, K_s$ and $m = 1, \ldots, M_s$ [29]. Here, $\mathbf{w}_T$ is a beamforming vector that, in the case of sensing, directs energy toward a specific direction, e.g., where a radar target is expected. Using a beam steering approach, the beamforming vector is expressed as

$$\mathbf{w}_T = \sqrt{\frac{P_k}{N_a}}\mathbf{a}(\theta, \psi) \tag{1}$$

where $P_k = P_T/K$ denotes the average transmit power per subcarrier, P_T is the total transmit power, and $\mathbf{a}(\theta, \psi) \in \mathbb{C}^{N_a\times 1}$ is the array response vector for the sensing directions (θ, ψ), characterizing the phase shifts across the antenna elements. For the considered URA, the steering vector is expressed as [30]

$$\mathbf{a}(\theta, \psi) = \mathbf{a}_x(\theta, \psi) \otimes \mathbf{a}_y(\theta, \psi). \tag{2}$$

The components along the x- and y-axes are given by

$$\mathbf{a}_x(\theta, \psi) = \left\{e^{-j\frac{2\pi}{\lambda}\frac{N_x-(2p-1)}{2}d_x u_x}\right\}_{p=1,\ldots,N_x} \in \mathbb{C}^{N_x\times 1} \tag{3}$$

$$\mathbf{a}_y(\theta, \psi) = \left\{e^{-j\frac{2\pi}{\lambda}\frac{N_y-(2q-1)}{2}d_y u_y}\right\}_{q=1,\ldots,N_y} \in \mathbb{C}^{N_y\times 1} \tag{4}$$

where $u_x = \sin(\theta)\cos(\psi)$ and $u_y = \sin(\theta)\sin(\psi)$.

A. RECEIVED SENSING SIGNAL

At the sensing receiver, backscattered signals from surrounding targets are collected. For each subcarrier k and OFDM symbol m, the received symbol vector $\mathbf{r}[k, m] \in \mathbb{C}^{N_a\times 1}$, after passing through the fast Fourier transform (FFT) block of the OFDM receiver, is given by[1]

$$\mathbf{r}[k, m] = \mathbf{H}[k, m]\mathbf{x}[k, m] + \boldsymbol{\nu}[k, m] \tag{5}$$

where ISI and inter-carrier interference (ICI) are assumed to be negligible. In (5), $\mathbf{H}[k, m] \in \mathbb{C}^{N_a\times N_a}$ represents the MIMO

[1]Note that monostatic radar operations rely on a full-duplex architecture, where analog and digital self-interference (SI) cancellation techniques are employed. A detailed characterization of the residual SI after cancellation, as well as its impact on sensing performance, lies outside the scope of this study. Accordingly, we assume that SI is sufficiently suppressed and can be considered negligible compared to the Gaussian noise.

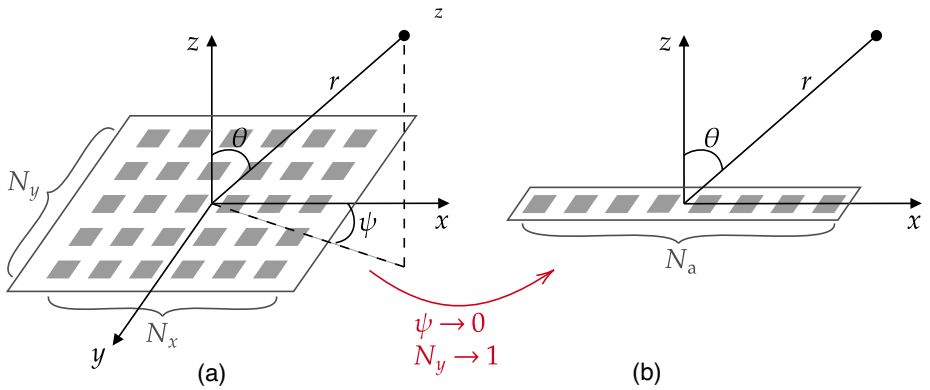

FIGURE 2. (a) URA with the reference system considered. (b) ULA as a limit case of the URA.

channel matrix for the kth subcarrier at time m, capturing the backscattering effects of surrounding targets. The term $\boldsymbol{\nu}[k,m] \sim \mathcal{CN}(\mathbf{0}, \sigma_\nu^2 \mathbf{I}_{N_a})$ denotes the additive white Gaussian noise (AWGN), modeled as a circularly symmetric complex Gaussian random vector. The noise samples $\boldsymbol{\nu}[k,m]$ are independent, identically distributed (i.i.d.) across subcarriers and time.

Consider reflections from a single point-like target at a distance r from the ISAC system and moving with a radial velocity v_r. Under far-field line-of-sight (LOS) propagation conditions, the channel matrix can be written as[2]

$$\mathbf{H}[k,m] = \alpha e^{j\phi} e^{j2\pi m T_\mathrm{s} f_\mathrm{D}} e^{-j2\pi k \Delta f \tau} \mathbf{b}(\theta,\psi)\mathbf{a}^\mathsf{H}(\theta,\psi) \quad (6)$$

where α is the channel gain, $\phi = -2\pi f_\mathrm{c}\tau$ is the common phase term, (θ,ψ) denotes both the direction of departure (DoD) and direction of arrival (DoA) of the target, τ represents the round-trip delay, and f_D is the Doppler shift. The latter are defined as

$$\tau = \frac{2r}{c} \quad (7)$$

$$f_\mathrm{D} = \frac{2v_\mathrm{r}}{\lambda} = \frac{2|\mathbf{v}|}{\lambda r} \times (x\sin\theta_\mathbf{v}\cos\psi_\mathbf{v} + y\sin\theta_\mathbf{v}\sin\psi_\mathbf{v} + z\cos\theta_\mathbf{v}) \quad (8)$$

where the vector $\mathbf{p} = (x,y,z)$ and $r = \|\mathbf{p}\|$ denote the target position vector and its distance from the origin of the coordinate system, respectively, while $\mathbf{v} = (|\mathbf{v}|, \theta_\mathbf{v}, \psi_\mathbf{v})$ represents the target velocity in spherical coordinates within a 3D space, and v_r denotes its radial velocity component. Moreover, $\mathbf{b}(\theta,\psi)$ is the receive array response vector corresponding to the DoA (θ, ψ), defined as in (2). According to the radar equation, the received power of the backscatter signal from the target is given by [31]

$$\alpha^2 = \frac{G_\mathrm{T} G_\mathrm{R} \sigma_\mathrm{rcs}\, c^2}{(4\pi)^3 f_\mathrm{c}^2\, r^4} \quad (9)$$

where σ_rcs is the target radar cross-section (RCS), while G_T and G_R are the single antenna element gains at the transmitter and receiver, respectively.

[2]The considered channel model neglects reflections from environmental clutter.

From the received signal in (5), we first remove the transmitted symbols $x_{k,m}$ (assumed to be known), which act as a nuisance parameter, by performing an element-wise division: $\mathbf{y}[k,m] = \mathbf{r}[k,m]/x_{k,m}$. As a result, for each (k,m) grid element, we obtain the noisy channel sample vector $\mathbf{y}[k,m] \in \mathbb{C}^{N_a \times 1}$, which can be written as

$$\mathbf{y}[k,m] = \alpha e^{j\phi} e^{j2\pi(mT_\mathrm{s}f_\mathrm{D} - k\Delta f\tau)} \mathbf{b}(\theta,\psi)\gamma + \mathbf{n}[k,m] \quad (10)$$

where $\mathbf{n}[k,m] \sim \mathcal{CN}(\mathbf{0}, \sigma_n^2 \mathbf{I}_N)$ is a circularly symmetric jointly Gaussian noise vector, with $\sigma_n^2 = \sigma_\nu^2 \cdot \mathbb{E}\{\frac{1}{|x_{k,m}|^2}\}$,[3] and $\gamma = \mathbf{a}^\mathsf{H}(\theta,\psi)\mathbf{w}_\mathrm{T}$ accounts for both the beamforming gain along the target direction and the transmit power.

Recalling that the noise after FFT blocks is white across the time, frequency, and spatial (antenna) domain, the log-likelihood function of the received ensemble $\boldsymbol{\mathcal{Y}} = \{\mathbf{y}[k,m]\}_{k=1,\dots,K_\mathrm{s},m=1,\dots,M_\mathrm{s}}$ is

$$\ln f\ (\boldsymbol{\mathcal{Y}}) = -\sum_{k=0}^{K_\mathrm{s}-1}\sum_{m=0}^{M_\mathrm{s}-1} N_\mathrm{a} \ln\left(\sigma_n^2\right) + \frac{1}{\sigma_n^2}\left\|\mathbf{y}[k,m] - \alpha e^{j\phi} e^{j2\pi m T_\mathrm{s} f_\mathrm{D}} e^{-j2\pi k\Delta f\tau}\mathbf{h}\right\|^2 \quad (11)$$

where we omitted those terms that are not relevant for the derivation of Fisher information matrix (FIM), and where $\mathbf{h} = \mathbf{b}(\theta,\psi)\gamma$.

III. POSITION ERROR BOUND

In the following, the CRLB expressions are computed with the coordinate system centered at the URA, so that potential errors in antenna location are not considered and the bounds are relative to this reference. This assumption suffices for analyzing resource allocation or antenna selection. If the absolute target position is of interest, the Bayesian CRLB should be employed to account for a priori distributions of the antenna location [32], [33]. Moreover, consistently

[3]Without loss of generality, we assume constant-envelope modulation, such as quadrature phase shift keying (QPSK), which implies $|x_{k,m}|^2 = 1$ for all k,m and thus $\sigma_n^2 = \sigma_\nu^2$. For other modulations, a correction factor on the noise variance should be applied after element-wise division [22].

with common practice in the CRLB literature, the analysis neglects residual SI and environmental clutter. The reported results should therefore be regarded as fundamental bounds that capture the performance limits imposed by system resources and target geometry, regardless of implementation impairments.

A. FISHER INFORMATION MATRIX AND CRLB

Given the vector of parameters $\mathbf{\Lambda} = [\alpha, \phi, f_{\mathrm{D}}, \tau, \theta, \psi]^{\mathsf{T}}$, the FIM is calculated from (11) as

$$[\mathcal{I}(\mathbf{\Lambda})]_{i,j} = -\mathbb{E}\left\{\frac{\partial^2 \ln f(\mathcal{Y})}{\partial\lambda_i \partial\lambda_j}\right\} \quad i,j \in \{1,\ldots,6\}. \tag{15}$$

After extensive but straightforward algebraic manipulation, the matrix $\mathcal{I}(\mathbf{\Lambda})$ presented in (12) at the bottom of this page can be derived.[4]

By inverting (12), we obtain the expression of the CRLB for the parameters of interest

$$\mathrm{CRLB}(\alpha) = \left[\mathcal{I}^{-1}\right]_{1,1} = \frac{\alpha^2}{2K_{\mathrm{s}}M_{\mathrm{s}}N_xN_y\mathrm{SNR}}$$
$$\mathrm{CRLB}(\phi) = \left[\mathcal{I}^{-1}\right]_{2,2} = \frac{7K_{\mathrm{s}}M_{\mathrm{s}} + K_{\mathrm{s}} + M_{\mathrm{s}} - 5}{2N_xN_y\left(K_{\mathrm{s}}^2 + K_{\mathrm{s}}\right)\left(M_{\mathrm{s}}^2 + M_{\mathrm{s}}\right)\mathrm{SNR}}$$
$$\mathrm{CRLB}(f_{\mathrm{D}}) = \left[\mathcal{I}^{-1}\right]_{3,3} = \frac{3}{2\pi^2K_{\mathrm{s}}M_{\mathrm{s}}N_xN_yT_{\mathrm{s}}^2\left(M_{\mathrm{s}}^2 - 1\right)\mathrm{SNR}}$$
$$\mathrm{CRLB}(\tau) = \left[\mathcal{I}^{-1}\right]_{4,4} = \frac{3}{2\pi^2K_{\mathrm{s}}M_{\mathrm{s}}N_xN_y\Delta f^2\left(K_{\mathrm{s}}^2 - 1\right)\mathrm{SNR}}$$
$$\mathrm{CRLB}(\theta) = \left[\mathcal{I}^{-1}\right]_{5,5} = \frac{\Upsilon_3}{2K_{\mathrm{s}}M_{\mathrm{s}}N_xN_y\left(\Upsilon_2^2 - \Upsilon_1\Upsilon_3\right)\mathrm{SNR}}$$
$$\mathrm{CRLB}(\psi) = \left[\mathcal{I}^{-1}\right]_{6,6} = \frac{\Upsilon_1}{2K_{\mathrm{s}}M_{\mathrm{s}}N_xN_y\left(\Upsilon_2^2 - \Upsilon_1\Upsilon_3\right)\mathrm{SNR}}$$

[4]A detailed derivation of the FIM elements in a 2D ISAC scenario with multiple cooperating BSs can be found in [22]. While the present work addresses a distinct 3D monostatic NTN-based setup, the reference may help readers follow the general methodology behind the derivations.

where we defined the signal-to-noise ratio (SNR) of the backscattered signal from the target per receiving antenna as [29]

$$\mathrm{SNR} = \frac{|\gamma|^2\alpha^2}{\sigma_v^2} = \frac{\Gamma(\theta,\psi)P_{\mathrm{k}}G_{\mathrm{T}}^{\mathrm{a}}G_{\mathrm{R}}\sigma_{\mathrm{rcs}}\,c^2}{(4\pi)^3 f_{\mathrm{c}}^2\, r^4 N_0 \Delta f} \tag{16}$$

where N_0 is the one-sided noise power spectral density (PSD), $G_{\mathrm{T}}^{\mathrm{a}} = N_{\mathrm{a}}G_{\mathrm{T}}$ is the transmit antenna array gain in the intended pointing direction, assuming perfect beam alignment. The factor $\Gamma(\theta,\psi) \in [0,1]$ accounts for any misalignment between the beamforming direction and the target. In this paper, we consider $\Gamma(\theta,\psi) = 1$ without loss of generality.

B. EQUIVALENT FISHER INFORMATION MATRIX AND PEB

The target position, $\mathbf{p}$, and its estimated counterpart, $\hat{\mathbf{p}}$, are defined with respect to the origin of the coordinate system, which corresponds with the center of the URA, as shown on the left-hand side of Fig. 2. Their respective representations in Cartesian coordinates are given by

$$\mathbf{p} = (x,y,z) = (r\sin(\theta)\cos(\psi), r\sin(\theta)\sin(\psi), r\cos(\theta))$$
$$\hat{\mathbf{p}} = (\hat{x},\hat{y},\hat{z}) = \left(\hat{r}\sin(\hat{\theta})\cos(\hat{\psi}), \hat{r}\sin(\hat{\theta})\sin(\hat{\psi}), \hat{r}\cos(\hat{\theta})\right).$$

The CRLB for the estimation of the target position in monostatic sensing can be calculated retaining only the information of the FIM (12) related to τ, θ, and ψ via the EFIM [34], [35]. The parameter vector $\mathbf{\Lambda}$ can be partitioned into $\mathbf{\Lambda} = [\mathbf{\Lambda}_1^{\mathsf{T}}, \mathbf{\Lambda}_2^{\mathsf{T}}]^{\mathsf{T}}$, with $\mathbf{\Lambda}_1 = [\alpha,\phi,f_{\mathrm{D}}]^{\mathsf{T}}$ and $\mathbf{\Lambda}_2 = [\tau,\theta,\psi]^{\mathsf{T}}$. This induces the partition of the FIM as

$$\mathcal{I}(\mathbf{\Lambda}) = \begin{bmatrix}\mathbf{A} & \mathbf{B}\\ \mathbf{B}^{\mathsf{T}} & \mathbf{C}\end{bmatrix} \tag{17}$$

where $\mathbf{A} \in \mathbb{R}^{3\times3}$, $\mathbf{B} \in \mathbb{R}^{3\times3}$, and $\mathbf{C} \in \mathbb{R}^{3\times3}$.

Then, the EFIM, also known as the Schur complement of $\mathbf{A}$, is given by [35]

$$\mathcal{I}_{\mathrm{e}}(\mathbf{\Lambda}_2) = \mathbf{C} - \mathbf{B}^{\mathsf{T}}\mathbf{A}^{-1}\mathbf{B} = \tag{18}$$

$$\mathcal{I}(\mathbf{\Lambda}) = 2K_{\mathrm{s}}M_{\mathrm{s}}\frac{\alpha^2||\mathbf{h}||^2}{\sigma_v^2} \times \begin{bmatrix} \frac{1}{\alpha^2} & 0 & 0 & 0 & 0 & 0\\ 0 & 1 & \pi T_{\mathrm{s}}(M_{\mathrm{s}}-1) & -\pi\Delta f(K_{\mathrm{s}}-1) & 0 & 0\\ 0 & \pi T_{\mathrm{s}}(M_{\mathrm{s}}-1) & 2\pi^2T_{\mathrm{s}}^2\frac{(2M_{\mathrm{s}}-1)(M_{\mathrm{s}}-1)}{3} & -\pi^2T_{\mathrm{s}}\Delta f(K_{\mathrm{s}}-1)(M_{\mathrm{s}}-1) & 0 & 0\\ 0 & -\pi\Delta f(K_{\mathrm{s}}-1) & -\pi^2T_{\mathrm{s}}\Delta f(K_{\mathrm{s}}-1)(M_{\mathrm{s}}-1) & 2\pi^2\Delta f^2\frac{(2K_{\mathrm{s}}-1)(K_{\mathrm{s}}-1)}{3} & 0 & 0\\ 0 & 0 & 0 & 0 & -\Upsilon_1 & -\Upsilon_2\\ 0 & 0 & 0 & 0 & -\Upsilon_2 & -\Upsilon_3 \end{bmatrix} \tag{12}$$

$$\Upsilon_1 = -\frac{\pi^2\cos^2(\theta)}{24}\left(-2 + N_x^2 + N_y^2 + \left(N_x^2 - N_y^2\right)\cos(2\psi)\right), \quad \Upsilon_2 = \frac{\pi^2}{48}\left(N_x^2 - N_y^2\right)\sin(2\psi)\sin(2\theta) \tag{13}$$

$$\Upsilon_3 = \frac{\pi^2\sin^2(\theta)}{24}\left(2 - N_x^2 - N_y^2 + \left(N_x^2 - N_y^2\right)\cos(2\psi)\right) \tag{14}$$

$$= 2K_sM_sN_xN_y\mathsf{SNR}\begin{bmatrix}\frac{1}{3}\pi^2\Delta f^2\left(K_s^2-1\right) & 0 & 0\\ 0 & -\Upsilon_1 & -\Upsilon_2\\ 0 & -\Upsilon_2 & -\Upsilon_3\end{bmatrix}.$$

Subsequently, reparameterization must be performed to calculate the EFIM for $\mathbf{p}$, that is defined as

$$[\mathcal{I}_e(\mathbf{p})]_{i,j} = -\mathbb{E}\left\{\frac{\partial^2 \ln f(\mathcal{Y})}{\partial p_i \partial p_j}\right\} \quad i,j \in \{1,2,3\}. \tag{19}$$

This can be obtained by the transformation

$$\mathcal{I}_e(\mathbf{p}) = \mathbf{J}_m^{\mathsf{T}}\mathcal{I}_e(\mathbf{\Lambda}_2)\mathbf{J}_m \tag{20}$$

where $\mathbf{J}_m$ is the Jacobian of the transformation $\{\tau = \frac{2}{c}\sqrt{x^2+y^2+z^2},\ \theta = \arccos(z/r),\ \psi = \arctan(y/x)\}$, which corresponds to

$$\mathbf{J}_m = \begin{bmatrix}\frac{\partial\tau}{\partial x} & \frac{\partial\tau}{\partial y} & \frac{\partial\tau}{\partial z}\\ \frac{\partial\theta}{\partial x} & \frac{\partial\theta}{\partial y} & \frac{\partial\theta}{\partial z}\\ \frac{\partial\psi}{\partial x} & \frac{\partial\psi}{\partial y} & \frac{\partial\psi}{\partial z}\end{bmatrix} \tag{21}$$

$$= \begin{bmatrix}\frac{2x}{c\sqrt{x^2+y^2+z^2}} & \frac{2y}{c\sqrt{x^2+y^2+z^2}} & \frac{2z}{c\sqrt{x^2+y^2+z^2}}\\ \frac{xz}{\sqrt{x^2+y^2}(x^2+y^2+z^2)} & \frac{yz}{\sqrt{x^2+y^2}(x^2+y^2+z^2)} & -\frac{\sqrt{x^2+y^2}}{x^2+y^2+z^2}\\ -\frac{y}{x^2+y^2} & \frac{x}{x^2+y^2} & 0\end{bmatrix}.$$

From (20) and by exploiting the cyclic property of the trace, the CRLB can be computed as

$$\mathsf{CRLB}(\mathbf{p}) = \mathrm{Tr}\left(\mathcal{I}_e^{-1}(\mathbf{p})\right) = \mathrm{Tr}\left(\mathcal{I}_e^{-1}(\mathbf{\Lambda}_2)\mathbf{M}\right) \tag{22}$$

with

$$\mathbf{M} = \left(\mathbf{J}_m^{-1}\right)^{\mathsf{T}}\mathbf{J}_m^{-1} = \mathrm{diag}\left(c^2/4, x^2+y^2+z^2, x^2+y^2\right). \tag{23}$$

After expanding the computation, a closed-form expression for the 3D-CRLB of the position estimate for the considered system can be obtained, as given in (26) at the bottom of the next page. Finally, from (26), we define the PEB as

$$\mathsf{PEB} = \sqrt{\mathsf{CRLB}(\mathbf{p})}. \tag{24}$$

It is worth noting that when considering a target positioned at $(0,0,z)$, a singularity arises in the $\mathsf{CRLB}(\mathbf{p})$ expression due to the indeterminate nature of ψ. To address this issue, we analyze the limit behavior as $(x,y) \to (0,0)$. The resulting limit is given by

$$\lim_{(x,y)\to(0,0)} \mathsf{CRLB}((x,y,z)) = \frac{1}{K_sM_sN_xN_y\mathsf{SNR}} \times\left(\frac{3c^2}{8\Delta f^2\left(K_s^2-1\right)\pi^2} + \frac{6\left(N_x^2+N_y^2-2\right)z^2}{\pi^2\left(N_x^2-1\right)\left(N_y^2-1\right)}\right). \tag{25}$$

C. REDUCTION OF THE 3D CRLB TO THE 2D CASE

In this subsection, we outline the procedure to reduce the bound derived in (26) to the 2D case presented in [28]. Since the 2D case can be obtained as a special case of the 3D scenario, we derive it via a limiting analysis.

Consider the URA where the dimensions are set as $N_x = N_a$ and $N_y \to 1$, while keeping the total number of antenna elements fixed at N_a. This configuration ensures that the URA collapses into a ULA, thereby restricting scanning to the xz-plane, as illustrated in Fig. 2b.

By plugging (13) and (14), shown at the bottom of the previous page, into (26), we observe that setting $N_y = 1$ leads to an indeterminate form in the CRLB expression. To resolve this, we apply L'Hôpital's rule, leading to the following bound

$$\lim_{N_y\to 1} \mathsf{CRLB}(\mathbf{p}) = \frac{1}{K_sM_sN_a\mathsf{SNR}} \times\left(\frac{3c^2}{8\Delta f^2\left(K_s^2-1\right)\pi^2} + \frac{6\left(\frac{r^2\cos^2(\psi)}{\cos^2(\theta)} + \frac{\left(x^2+y^2\right)\sin^2(\psi)}{\sin^2(\theta)}\right)}{\left(N_a^2-1\right)\pi^2}\right). \tag{27}$$

The final 2D bound is obtained by evaluating the limit of the second term in (27) as $\psi \to 0$, yielding

$$\lim_{\psi\to 0}\left(\lim_{N_y\to 1}\mathsf{CRLB}(\mathbf{p})\right) = \frac{1}{\pi^2K_sM_sN_a\mathsf{SNR}} \times\left(\frac{3c^2}{8\Delta f^2\left(K_s^2-1\right)} + \frac{6\left(x^2+z^2\right)}{\left(N_a^2-1\right)\cos^2(\theta)}\right) \tag{28}$$

which matches the expression provided in [28, eq. (18)].

IV. VELOCITY ERROR BOUND

In the considered monostatic 3D ISAC scenario, the inability to observe Doppler shifts in multiple independent spatial directions prevents the estimation of the full target velocity vector. However, if the direction of the target's motion is known a priori (i.e., the angles $\theta_{\mathbf{v}}$ and $\psi_{\mathbf{v}}$ that define the orientation of the velocity vector are available), it becomes possible to compute the CRLB on the velocity magnitude, whose square root is hereinafter referred to as the VEB.

A practical example is that of a UAV performing sensing operations over a road, where the direction of vehicle motion is known due to road geometry, and the goal is to estimate only the velocity magnitude of the targets. Such scenarios are particularly relevant in automotive and aerial surveillance applications, where partial prior knowledge can be leveraged to enhance estimation performance.

To derive the VEB, we define the Jacobian $\mathbf{J}_\Omega$ of the transformation $\Omega : (x,y,z,|\mathbf{v}|) \to (f_D,\tau,\theta,\psi)$ as

$$\mathbf{J}_\Omega = \begin{bmatrix}\frac{\partial f_D}{\partial x} & \frac{\partial f_D}{\partial y} & \frac{\partial f_D}{\partial z} & \frac{\partial f_D}{\partial|\mathbf{v}|}\\ \frac{\partial\tau}{\partial x} & \frac{\partial\tau}{\partial y} & \frac{\partial\tau}{\partial z} & \frac{\partial\tau}{\partial|\mathbf{v}|}\\ \frac{\partial\theta}{\partial x} & \frac{\partial\theta}{\partial y} & \frac{\partial\theta}{\partial z} & \frac{\partial\theta}{\partial|\mathbf{v}|}\\ \frac{\partial\psi}{\partial x} & \frac{\partial\psi}{\partial y} & \frac{\partial\psi}{\partial z} & \frac{\partial\psi}{\partial|\mathbf{v}|}\end{bmatrix} = \begin{bmatrix}\frac{\partial f_D}{\partial x} & \frac{\partial f_D}{\partial y} & \frac{\partial f_D}{\partial z} & \frac{\partial f_D}{\partial|\mathbf{v}|}\\ \left[\begin{matrix}\\ \mathbf{J}_m\\ \\ \end{matrix}\right] & & & \begin{matrix}0\\0\\0\end{matrix}\end{bmatrix} \tag{33}$$

where the frequency Doppler derivatives, computed from (8), are provided in (29)-(32) at the bottom of the next page and $\mathbf{J}_m$ is given in (21).

We aim now to derive the EFIM of joint velocity and position estimation. Similar to the procedure illustrated in Section III, we partition the parameter vector $\boldsymbol{\Lambda} = [\alpha, \phi, f_{\mathrm{D}}, \tau, \theta, \psi]^{\mathrm{T}}$ into $\boldsymbol{\Lambda} = [\boldsymbol{\Lambda}_1^{\mathrm{T}}, \boldsymbol{\Lambda}_2^{\mathrm{T}}]^{\mathrm{T}}$ with $\boldsymbol{\Lambda}_1 = [\alpha, \phi]^{\mathrm{T}}$ $\boldsymbol{\Lambda}_2 = [f_{\mathrm{D}}, \tau, \theta, \psi]^{\mathrm{T}}$, which induces the partition of the FIM as (17), where $\mathbf{A} \in \mathbb{R}^{2\times 2}$, $\mathbf{B} \in \mathbb{R}^{2\times 4}$, and $\mathbf{C} \in \mathbb{R}^{4\times 4}$. By computed the Schur complement of $\mathbf{A}$ we get the EFIM, as follows

$$\boldsymbol{\mathcal{I}}_{\mathrm{e}}(\boldsymbol{\Lambda}_2) = \mathbf{C} - \mathbf{B}^{\mathrm{T}}\mathbf{A}^{-1}\mathbf{B} = 2K_{\mathrm{s}}M_{\mathrm{s}}N_xN_y\mathsf{SNR} \times \begin{bmatrix} \frac{1}{3}\pi^2 T_{\mathrm{s}}^2\left(M_{\mathrm{s}}^2-1\right) & 0 & 0 & 0 \\ 0 & \frac{1}{3}\pi^2\Delta f^2\left(K_{\mathrm{s}}^2-1\right) & 0 & 0 \\ 0 & 0 & -\Upsilon_1 & -\Upsilon_2 \\ 0 & 0 & -\Upsilon_2 & -\Upsilon_3 \end{bmatrix}. \tag{34}$$

Next, we perform reparameterization to calculate the EFIM for the set of parameters $(x, y, z, |\mathbf{v}|)$. This can be obtained by the transformation

$$\boldsymbol{\mathcal{I}}_{\mathrm{e}}(x, y, z, |\mathbf{v}|) = \mathbf{J}_{\Omega}^{\mathrm{T}}\boldsymbol{\mathcal{I}}_{\mathrm{e}}(\boldsymbol{\Lambda}_2)\mathbf{J}_{\Omega} = \begin{bmatrix} \boldsymbol{\mathcal{I}}_{\mathrm{p}} & \boldsymbol{\mathcal{I}}_{\mathrm{pv}} \\ \boldsymbol{\mathcal{I}}_{\mathrm{pv}}^{\mathrm{T}} & \mathcal{I}_{\mathrm{v}} \end{bmatrix} \tag{35}$$

where $\mathbf{J}_{\Omega}$ is given in (33), $\boldsymbol{\mathcal{I}}_{\mathrm{p}} \in \mathbb{R}^{3\times 3}$ retains information about $\mathbf{p}$, $\mathcal{I}_{\mathrm{v}}$ captures information about $\mathbf{v}$, and $\boldsymbol{\mathcal{I}}_{\mathrm{pv}} \in \mathbb{R}^{3\times 1}$ represents the position-velocity cross-information.

Treating the position $\mathbf{p}$ as nuisance parameters, the local EFIM for the magnitude $|\mathbf{v}|$ of the target velocity is obtained by computing the Schur complement of $\boldsymbol{\mathcal{I}}_{\mathrm{p}}$

$$I_{\mathrm{e}}(|\mathbf{v}|) = \mathcal{I}_{\mathrm{v}} - \boldsymbol{\mathcal{I}}_{\mathrm{pv}}^{\mathrm{T}}\boldsymbol{\mathcal{I}}_{\mathrm{p}}^{-1}\boldsymbol{\mathcal{I}}_{\mathrm{pv}}. \tag{36}$$

Then, by inverting $I_{\mathrm{e}}(|\mathbf{v}|)$, we obtain the expression of the CRLB for the parameter $|\mathbf{v}|$ given in (39) at the bottom of the next page. The VEB is then defined as

$$\mathrm{VEB} = \sqrt{\mathsf{CRLB}(|\mathbf{v}|)}. \tag{37}$$

Remark 1: For certain configurations, the expression of the velocity CRLB can be simplified. As an illustrative example, consider a scenario in which a UAV performs sensing operations directed toward the ground. Under the assumption that targets move on a 2D plane, the velocity angle $\theta_{\mathbf{v}}$ can be fixed to $\pi/2$. In this specific case, assuming $N_x = N_y$, the CRLB simplifies to

$$\begin{aligned}\mathsf{CRLB}(|\mathbf{v}|) &= \frac{3r^2}{\epsilon\pi^2}\left(\frac{\lambda^2}{8T_{\mathrm{s}}^2\left(M_{\mathrm{s}}^2-1\right)} - \frac{2|\mathbf{v}|^2}{1-\sqrt{N_{\mathrm{a}}}}\right) \\ &= \frac{3|\mathbf{v}|^2}{\pi^2 v_{\mathrm{r}}^2 K_{\mathrm{s}}M_{\mathrm{s}}N_xN_y\mathsf{SNR}}\left(\frac{\lambda^2}{8T_{\mathrm{s}}^2\left(M_{\mathrm{s}}^2-1\right)} - \frac{2|\mathbf{v}|^2}{1-\sqrt{N_{\mathrm{a}}}}\right)\end{aligned} \tag{38}$$

where the expression of ϵ in (40), shown at the bottom of the next page, has been made explicit.

Remark 2: It is important to note that we assume ground targets move along known directions, which is a valid assumption in structured road-monitoring scenarios. However, in situations where this assumption does not hold–such as at intersections, during lane changes, or due to unexpected maneuvers–the monostatic setup exhibits inherent limitations. In particular, although target positions can still be estimated, velocity estimation becomes infeasible, since a monostatic system, without any prior knowledge, can only measure the radial velocity component rather than the full velocity vector. To overcome this limitation, cooperation among multiple UAVs can be exploited [22].

V. CRLB-BASED UAV SELECTION FROM A FLEET

The use of UAV fleets enables collaborative operation, where multiple drones can dynamically share roles between sensing the environment and providing communication services. A principled approach to designing and optimizing such fleets requires a rigorous understanding of the fundamental performance limits of sensing tasks. In the previous sections, we have computed the CRLBs on position and velocity estimation errors for a monostatic 3D MIMO-OFDM ISAC system. These bounds provide essential performance benchmarks that can inform strategic decisions in UAV fleet management.

Consider a fleet of N_{u} UAVs, from which one must be selected to perform a sensing task aimed at localizing a target positioned at $\mathbf{p}_g = (x_g, y_g, z_g)$ and moving with velocity $\mathbf{v}$. In contrast to the previous sections, where a local coordinate system centered at the URA of a single UAV was adopted,

$$\mathsf{CRLB}(\mathbf{p}) = \frac{c^2}{4}\left[\boldsymbol{\mathcal{I}}^{-1}\right]_{4,4} + r^2\left[\boldsymbol{\mathcal{I}}^{-1}\right]_{5,5} + \left(x^2+y^2\right)\left[\boldsymbol{\mathcal{I}}^{-1}\right]_{6,6} = \frac{1}{K_{\mathrm{s}}M_{\mathrm{s}}N_xN_y\mathsf{SNR}}\left(\frac{3c^2}{8\Delta f^2\left(K_{\mathrm{s}}^2-1\right)\pi^2} + \frac{r^2\Upsilon_3 + \left(x^2+y^2\right)\Upsilon_1}{2\left(\Upsilon_2^2 - \Upsilon_1\Upsilon_3\right)}\right) \tag{26}$$

$$\frac{\partial f_{\mathrm{D}}}{\partial x} = \frac{2|\mathbf{v}|}{\lambda}\frac{\sin(\theta_{\mathbf{v}})\cos(\psi_{\mathbf{v}})\left(y^2+z^2\right) - \sin(\theta_{\mathbf{v}})\sin(\psi_{\mathbf{v}})xy - \cos(\theta_{\mathbf{v}})xz}{r^3} \tag{29}$$

$$\frac{\partial f_{\mathrm{D}}}{\partial y} = \frac{2|\mathbf{v}|}{\lambda}\frac{\sin(\theta_{\mathbf{v}})\sin(\psi_{\mathbf{v}})\left(x^2+z^2\right) - y(\sin(\theta_{\mathbf{v}})\cos(\psi_{\mathbf{v}})x + \cos(\theta_{\mathbf{v}})z)}{r^3} \tag{30}$$

$$\frac{\partial f_{\mathrm{D}}}{\partial z} = \frac{2|\mathbf{v}|}{\lambda}\frac{\cos(\theta_{\mathbf{v}})\left(x^2+y^2\right) - z(\sin(\theta_{\mathbf{v}})\cos(\psi_{\mathbf{v}})x + \sin(\theta_{\mathbf{v}})\sin(\psi_{\mathbf{v}})y)}{r^3} \tag{31}$$

$$\frac{\partial f_{\mathrm{D}}}{\partial |\mathbf{v}|} = \frac{2}{\lambda}\frac{x\,\sin(\theta_{\mathbf{v}})\cos(\psi_{\mathbf{v}}) + y\,\sin(\theta_{\mathbf{v}})\sin(\psi_{\mathbf{v}}) + z\,\cos(\theta_{\mathbf{v}})}{r} \tag{32}$$

we now shift to a global reference frame appropriate for system-level analysis involving multiple UAVs. Within this global frame, the position of the ith UAV is denoted by the vector $\mathbf{p}_{\text{uav}}^{(i)} = [x_{\text{uav}}^{(i)}, y_{\text{uav}}^{(i)}, z_{\text{uav}}^{(i)}]$, and the set of all UAV positions is defined as $\mathcal{S} = \{\mathbf{p}_{\text{uav}}^{(1)}, \ldots, \mathbf{p}_{\text{uav}}^{(N_{\text{u}})}\}$.

For each UAV, the position of the target can be expressed in the UAV's local coordinate frame. Specifically, for the ith UAV, the local coordinates of the target are given by $\mathbf{p}^{(i)} = (x^{(i)}, y^{(i)}, z^{(i)})$, where[5]

$$x^{(i)} = -\left(x_g - x_{\text{uav}}^{(i)}\right),\ y^{(i)} = y_g - y_{\text{uav}}^{(i)},\ z^{(i)} = -\left(z_g - z_{\text{uav}}^{(i)}\right).$$

Let $\mathcal{B}(\mathbf{p}_{\text{uav}}^{(i)})$ denote a chosen performance metric derived from the CRLBs, either the PEB derived from $\mathsf{CRLB}(\mathbf{p}^{(i)})$ (eq. (26)) or the VEB derived from $\mathsf{CRLB}(|\mathbf{v}|)$ (eq. (39)). The optimal sensing UAV is selected by solving the following minimization problem:

$$\left(x_{\text{uav}}^*, y_{\text{uav}}^*, z_{\text{uav}}^*\right) = \arg\min_{\mathbf{p}_{\text{uav}}^{(i)} \in \mathcal{S}} \mathcal{B}\left(\mathbf{p}_{\text{uav}}^{(i)}\right) \tag{41}$$

where $\mathbf{p}_{\text{uav}}^* = [x_{\text{uav}}^*, y_{\text{uav}}^*, z_{\text{uav}}^*]$ denotes the position of the UAV selected to minimize the chosen performance bound. For moderate values of N_{u}, this problem can be efficiently solved via exhaustive search over all candidate UAVs.

It is worth emphasizing the difference between UAV selection and UAV placement. In practical ISAC scenarios, UAV positions are typically constrained by communication objectives and by regulatory frameworks such as AHs, which impose predefined aerial corridors. Therefore, in this work, we consider a monostatic ISAC setup where a fleet of UAVs is already deployed primarily to meet communication requirements. In this context, the problem is not to optimize deployment for sensing, but rather to select, within the available fleet, the UAV that yields the best sensing performance according to the CRLB. This differs from UAV placement, where optimal sensor locations are determined to minimize the CRLB [36]. Although [36] focuses on the latter scenario, its mathematical framework can also provide a useful tool for evaluating the quality of different subsets of available UAVs. Since the scenario considered here is relatively simple, this powerful tool is not used in the present work.

[5]The transformation from global to local coordinates involves a translation followed by a reflection across the x-y plane, effectively flipping the x and z axes. This reflects the physical configuration in which the global reference frame is grounded and oriented upwards, while each UAV's local frame is oriented downwards, with its sensing apparatus (e.g., the URA) facing the ground. The resulting transformation ensures that the target appears in front of the URA (i.e., $z^{(i)} > 0$) when expressed in the UAV's local frame. This convention simplifies the analysis by aligning the sensing direction with the positive z-axis in the local frame.

TABLE 2. System parameters.

Parameter	Value	Parameter	Value
OFDM symbols per frame M	1120	Active subcarriers K	3168
OFDM symbol duration T_{s}	$8.92\,\mu$s	Subcarrier spacing Δf	120 kHz
Carrier frequency f_{c}	28 GHz	Total OFDM power P_{T}	30 dBm
Power per subcarrier P_{k}	-5 dBm	Noise PSD N_0	$4 \cdot 10^{-20}$ W/Hz
Target RCS σ_{RCS}	1 m^2	Target speed $\lvert\mathbf{v}\rvert$	27 m/s

VI. NUMERICAL RESULTS

In this section, we consider the presence of a UAV designed for environmental sensing and assess the target localization accuracy in terms of PEB and velocity estimation accuracy in terms of VEB. For all the simulations, 5G new radio (NR) signals compliant with 3GPP Technical Specification in [37] are considered. The system transmits QPSK modulation symbols by employing a carrier frequency of $f_{\text{c}} = 28$ GHz, a total transmit power $P_{\text{T}} = 30$ dBm, number of total subcarrier $K = 3168$ (i.e., a total bandwidth of around 400 MHz), and subcarrier spacing $\Delta f = 120$ kHz. Each OFDM symbol has a total duration $T_{\text{s}} = 8.92\,\mu$s. The number of OFDM symbols M_{s} and the number of subcarriers K_{s} used for sensing purposes are specified in each simulation. The system parameters are summarized in Table 2.

The RCS of the target is given by $\sigma_{\text{RCS}} = 1\,\text{m}^2$. The noise PSD is expressed as $N_0 = k_{\text{B}} T_0 F$, where $k_{\text{B}} = 1.38 \cdot 10^{-23}\,\text{JK}^{-1}$ denotes the Boltzmann constant, $T_0 = 290$ K represents the reference temperature, and the receiver noise figure is $F_{\text{dB}} = 10$ dB.

In the Sections VI-A and VI-B, the origin of the coordinate system is assumed to be at the center of the URA. Consequently, all target position vectors $\mathbf{p}$ are expressed with respect to this reference system. Contrariwise, in the last Section VI-C, we consider a global coordinate system as mentioned in Section V.

A. PEB VS SYSTEM PARAMETERS

Fig. 3 presents the PEB as a function of the number of subcarriers K_{s} used for sensing, considering different antenna

$$\mathsf{CRLB}(|\mathbf{v}|) = I_{\text{e}}^{-1}(|\mathbf{v}|) = \frac{3\lambda^2 r^2}{8\epsilon\pi^2 T_{\text{s}}^2 (M_{\text{s}}^2 - 1)} + \frac{|\mathbf{v}|^2}{\epsilon\left(\Upsilon_2^2 - \Upsilon_3\Upsilon_1\right)} \tag{39}$$
$$\times \left[\frac{\Upsilon_2 \sin^2(\theta_{\mathbf{v}})\left(xyz\cos(2\psi_{\mathbf{v}}) - \frac{1}{4}z(x^2 - y^2)\sin(2\psi_{\mathbf{v}})\right)}{\sqrt{x^2 + y^2}} + \frac{\Upsilon_1 \sin^2(\theta_{\mathbf{v}})(\cos(\psi_{\mathbf{v}})y - \sin(\psi_{\mathbf{v}})x)^2}{2} + \frac{\Upsilon_3 z^2 \sin^2(\theta_{\mathbf{v}})(\cos(\psi_{\mathbf{v}})x + \sin(\psi_{\mathbf{v}})y)^2}{2(x^2 + y^2)}\right.$$
$$\left. + \frac{1}{2}\left(\Upsilon_2\sqrt{x^2 + y^2}\sin(2\theta_{\mathbf{v}})(\sin(\psi_{\mathbf{v}})x - \cos(\psi_{\mathbf{v}})y) - \Upsilon_3 z\sin(2\theta_{\mathbf{v}})(\cos(\psi_{\mathbf{v}})x + \sin(\psi_{\mathbf{v}})y) + \Upsilon_3\cos^2(\theta_{\mathbf{v}})\left(x^2 + y^2\right)\right)\right]$$

$$\epsilon = K_{\text{s}} M_{\text{s}} N_x N_y \mathsf{SNR}(x\,\sin(\theta_{\mathbf{v}})\cos(\psi_{\mathbf{v}}) + y\,\sin(\theta_{\mathbf{v}})\sin(\psi_{\mathbf{v}}) + z\,\cos(\theta_{\mathbf{v}}))^2 \tag{40}$$

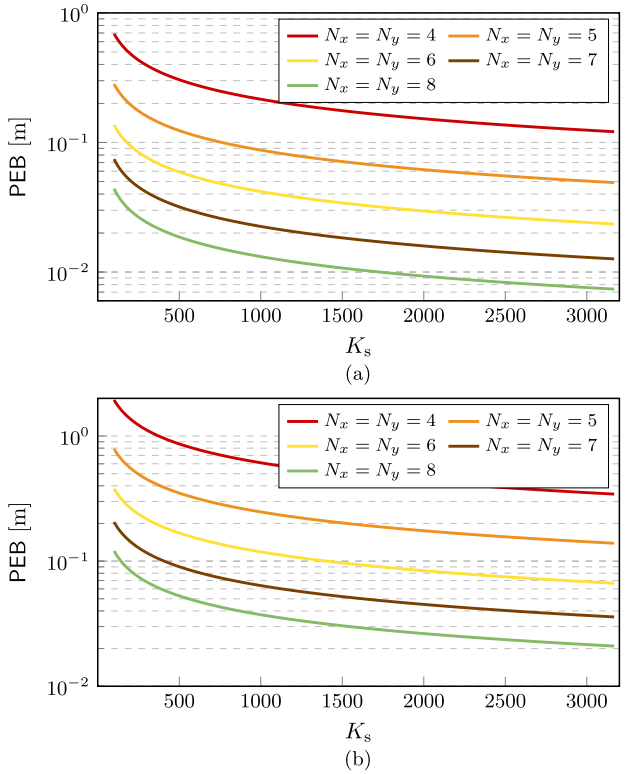

FIGURE 3. PEB as a function of the number of subcarriers K_s and different antenna array sizes. (a) Curves obtained for target position $\mathbf{p} = (0, 0, 100)$ m. (b) Curves obtained for target position $\mathbf{p} = (-55, 70, 100)$ m.

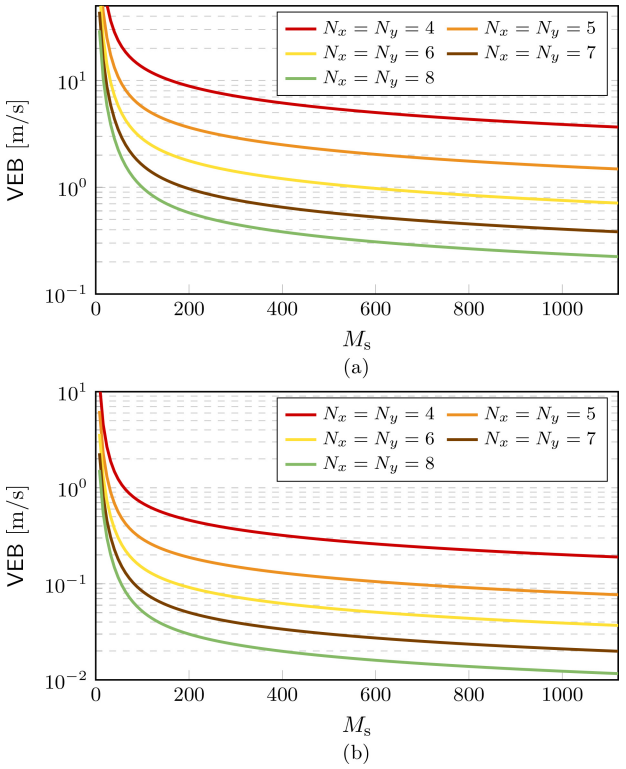

FIGURE 4. VEB as a function of the number of OFDM symbols M_s and different antenna array sizes. (a) Curves obtained for target position $\mathbf{p} = (-2, 0, 100)$ m. (b) Curves obtained for target position $\mathbf{p} = (50, 50, 100)$ m.

array sizes. For this analysis, the number of OFDM symbols is set to $M_s = 112$.

In Fig. 3a, the target is positioned directly below the UAV at $\mathbf{p} = (0, 0, 100)$ m, whereas in Fig. 3b, it is located at $\mathbf{p} = (-55, 70, 100)$ m.[6] As expected from (26), the results confirm that increasing the number of subcarriers leads to lower PEB values. A similar trend is observed when increasing the number of URA antenna elements, N_x and N_y, further enhancing localization accuracy.

In particular, these curves illustrate the significant impact of the number of antennas on localization accuracy compared to the system bandwidth, emphasizing the critical role of direction of arrival estimation. Specifically, referring to Fig. 3a, the best achievable PEB with a 16-antenna array is approximately 10 cm when using a 400 MHz bandwidth. In contrast, increasing the array size to 64 antennas enables a PEB below 1 cm with only 200 MHz of bandwidth. This result aligns with previous findings on 2D bounds, such as those presented in [28].

B. VEB VS SYSTEM PARAMETERS

Fig. 4 presents the VEB as a function of the number of OFDM symbols M_s used for sensing, considering different antenna array sizes. In Fig. 4a, the target is positioned near the UAV at $\mathbf{p} = (-2, 0, 100)$ m, whereas in Fig. 4b, it is located at $\mathbf{p} = (50, 50, 100)$ m. All results are averaged over 2×10^3 Monte Carlo iterations using $K_s = 636$ subcarriers. In each iteration, the velocity angle $\psi_{\mathbf{v}}$ is randomly drawn from the interval $(0, 2\pi)$, while the velocity magnitude is fixed at 27 m/s and the direction $\theta_{\mathbf{v}}$ is set at $\pi/2$.[7] The results confirm that increasing the number of OFDM symbols yields lower VEB values. A similar improvement in velocity estimation accuracy is observed as the number of URA elements, N_x and N_y, increases. Interestingly, among the two simulated target positions, a lower VEB is achieved when the target is located farther from the UAV, likely due to the more favorable geometry of the scenario in that configuration. This observation is consistent with the expression of $\mathsf{CRLB}(|\mathbf{v}|)$ in (39), which reveals a strong dependence on the target's x and y coordinates.

C. CRLB-BASED PERFORMANCE EVALUATION FOR UAV SELECTION

Fig. 5 presents a system-level analysis based on both the PEB and VEB, following the CRLB-based UAV selection strategy introduced in Section V.

We consider a scenario where a target moves along a horizontal trajectory from $\mathbf{p}_g = (-50, 10, 0)$ m to $\mathbf{p}_g =$

[6]Note that for the analysis of Fig. 3a, the CRLB expression in (25) is applied, as the target is located along the z-axis.

[7]Due to the system geometry, certain values of $\psi_{\mathbf{v}}$ result in a null radial velocity component, leading to a divergence of the $\mathrm{CRLB}(|\mathbf{v}|)$ to infinity. To ensure meaningful performance evaluation, these cases are excluded from the Monte Carlo simulations.

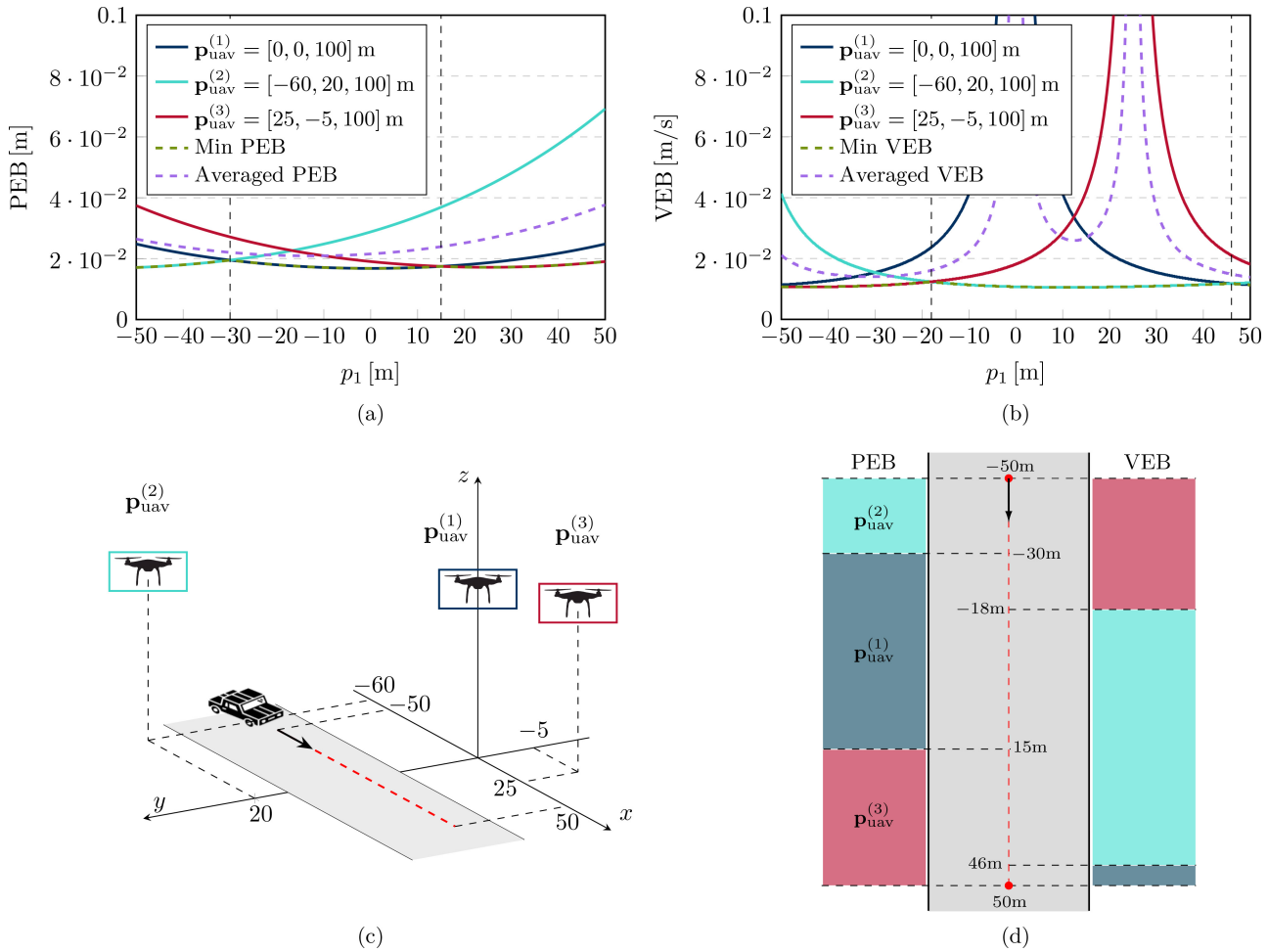

FIGURE 5. Comparison of the PEB and VEB for different UAV deployment configurations. The target moves along a horizontal trajectory from (−50, 10, 0) m to (50, 10, 0) m. (a)-(b) PEB and VEB, respectively, as functions of the target's x-coordinate p_1 in the global reference frame, for three distinct UAV positions. (c) Simulated environment, where the red dashed line represents the target's trajectory. (d) Different colors along the road indicate the optimal UAV–among the three candidates–to minimize the corresponding error bound at each point along the trajectory.

(50, 10, 0) m at a constant speed of 100 km/h in the direction of the x-axis, i.e., $(\theta_{\mathbf{v}}, \psi_{\mathbf{v}}) = (\pi/2, 0)$. The area is monitored by three UAVs as shown in Fig. 5c. Each URA is composed of $N_x = N_y = 8$ antenna elements and sensing is performed using $K_{\text{s}} = 636$ subcarriers and $M_{\text{s}} = 112$ OFDM symbols. For each UAV, the position and velocity estimation bounds are evaluated along the trajectory and depicted in Fig. 5a and Fig. 5b, where the x-axis variable p_1 represents the target's x-coordinate in the global reference frame.[8] The dashed curves correspond to the minimum bound achievable in the considered scenario and the averaged bound across all UAVs. The results clearly show that the minimum bound can be significantly tighter than the average, highlighting the performance gains enabled by the proposed selection strategy.

[8]As previously noted, all coordinates in this subsection are expressed in the global reference frame. However, to compute the bounds, the target's global coordinates are transformed into the local reference frame centered at the URA of each UAV, as described in Section V

At the beginning of the trajectory, the highest position estimation accuracy is achieved when the UAV is located at $\mathbf{p}_{\text{uav}}^{(2)} = [-60, 20, 100]$ m, likely because this is the closest UAV to the target. In contrast, the lowest VEB is obtained when the UAV is positioned at $\mathbf{p}_{\text{uav}}^{(3)} = [25, -5, 100]$ m, which is the farthest. As the target progresses along its trajectory, this trend reverses: the PEB reaches its minimum for the UAV located at $\mathbf{p}_{\text{uav}}^{(3)}$, whereas the lowest VEB is observed for the UAV at $\mathbf{p}_{\text{uav}}^{(2)}$.

Fig. 5b shows that when the target is located at $\mathbf{p}_g = (0, 10, 0)$ m and the UAV is positioned at $\mathbf{p}_{\text{uav}}^{(1)} = [0, 0, 100]$ m, the resulting VEB is significantly large. This can be explained by observing that, when expressing the target's position in the local reference frame centered at this UAV, we obtain $\mathbf{p}^{(1)} = (0, 10, 100)$ m, leading to a null radial velocity component. Specifically, the expression

$$v_{\text{r}} = |\mathbf{v}|\Big(x^{(1)} \sin(\theta_{\mathbf{v}}) \cos(\psi_{\mathbf{v}}) + y^{(1)} \sin(\theta_{\mathbf{v}}) \sin(\psi_{\mathbf{v}}) + z^{(1)} \cos(\theta_{\mathbf{v}})\Big)$$

evaluates to zero in this configuration. As a consequence, the UAV is unable to observe any radial motion and, therefore, cannot reliably estimate the magnitude of the target's velocity. A similar phenomenon is observed for the UAV at $\mathbf{p}_{\text{uav}}^{(3)} = [25, -5, 100]$ m when the target is at position $\mathbf{p}_g = (25, 10, 0)$ m.

Finally, Fig. 5d shows the optimal UAV assignment along the trajectory based on the selected performance metric. Notably, minimizing the PEB and the VEB leads to different UAV selections, highlighting the importance of aligning the UAV assignment strategy with the specific estimation objective.

VII. CONCLUSION

In this work, we derived and analyzed the fundamental limits of 3D target localization and velocity estimation accuracy in a monostatic OFDM-based ISAC system. A unified analytical framework was developed to evaluate positioning performance using the PEB metric, demonstrating that the derived 3D CRLB naturally includes the 2D case as a special instance. Additionally, we provided a closed-form expression for the VEB under a realistic scenario where a UAV senses a ground-based target with known velocity orientation. Our numerical evaluations underscore the advantages of increasing system resources, such as bandwidth, number of OFDM symbols, and the number of antenna elements in the URA, in enhancing estimation performance. Finally, we illustrated how these theoretical bounds can support system-level decision-making, for instance by guiding the selection of the most suitable BS for sensing in a specific region.

Future research could leverage the CRLB expressions in (26) and (39) within specific application scenarios to enable optimized network management and resource allocation.

REFERENCES

[1] N. González-Prelcic et al., "The integrated sensing and communication revolution for 6G: Vision, techniques, and applications," *Proc. IEEE*, vol. 112, no. 7, pp. 676–723, Jul. 2024.

[2] E. Matricardi, E. Favarelli, L. Pucci, W. Xu, E. Paolini, and A. Giorgetti, "Toward intelligent roads: Uniting sensing and communication in mobile networks," *Sensors*, vol. 25, no. 3, p. 778, 2025.

[3] N. Decarli, S. Bartoletti, A. Bazzi, R. A. Stirling-Gallacher, and B. M. Masini, "Performance characterization of joint communication and sensing with beyond 5G NR-V2X sidelink," *IEEE Trans. Veh. Technol.*, vol. 73, no. 7, pp. 10044–10059, Jul. 2024.

[4] C. Baquero Barneto et al., "Full-duplex OFDM radar with LTE and 5G NR waveforms: Challenges, solutions, and measurements," *IEEE Trans. Microw. Theory Techn.*, vol. 67, no. 10, pp. 4042–4054, Oct. 2019.

[5] C. Sturm and W. Wiesbeck, "Waveform design and signal processing aspects for fusion of wireless communications and radar sensing," *Proc. IEEE*, vol. 99, no. 7, pp. 1236–1259, Jul. 2011.

[6] M. Braun, C. Sturm, and F. K. Jondral, "Maximum likelihood speed and distance estimation for OFDM radar," in *Proc. IEEE Radar Conf.*, Arlington, VA, USA, May 2010, pp. 256–261.

[7] E. G. Larsson, O. Edfors, F. Tufvesson, and T. L. Marzetta, "Massive MIMO for next generation wireless systems," *IEEE Commun. Mag.*, vol. 52, no. 2, pp. 186–195, Feb. 2014.

[8] T. S. Rappaport et al., "Millimeter wave mobile communications for 5G cellular: It will work!" *IEEE Access*, vol. 1, pp. 335–349, 2013.

[9] G. Huang et al., "A novel multi-beam directional modulation OFDM waveform design for integrated sensing and communication," *IEEE Trans. Veh. Technol.*, early access, Jun. 3, 2025, doi: 10.1109/TVT.2025.3576252.

[10] M. M. Saad, M. A. Tariq, M. T. R. Khan, and D. Kim, "Non-terrestrial networks: An overview of 3GPP release 17 & 18," *IEEE Internet Things Mag.*, vol. 7, no. 1, pp. 20–26, Jan. 2024.

[11] L. Spampinato, D. Ferretti, C. Buratti, and R. Marini, "Joint trajectory design and radio resource management for UAV-aided vehicular networks," *IEEE Trans. Veh. Technol.*, vol. 74, no. 1, pp. 847–860, Jan. 2025.

[12] K. Meng et al., "UAV-enabled integrated sensing and communication: Opportunities and challenges," *IEEE Wireless Commun.*, vol. 31, no. 2, pp. 97–104, Apr. 2024.

[13] Z. Liu, X. Liu, Y. Liu, V. C. M. Leung, and T. S. Durrani, "UAV assisted integrated sensing and communications for Internet of Things: 3D trajectory optimization and resource allocation," *IEEE Trans. Wireless Commun.*, vol. 23, no. 8, pp. 8654–8667, Aug. 2024.

[14] M. Elloumi, R. Dhaou, B. Escrig, H. Idoudi, and L. A. Saidane, "Monitoring road traffic with a UAV-based system," in *Proc. IEEE Wireless Comm. and Net. Conf. (WCNC)*, Barcelona, Spain, Apr. 2018, pp. 1–6.

[15] X. Kong, C. Ni, G. Duan, G. Shen, Y. Yang, and S. K. Das, "Energy consumption optimization of UAV-assisted traffic monitoring scheme with tiny reinforcement learning," *IEEE Internet Things J.*, vol. 11, no. 12, pp. 21135–21145, Jun. 2024.

[16] N. Cherif, W. Jaafar, H. Yanikomeroglu, and A. Yongacoglu, "3D aerial highway: The key enabler of the retail industry transformation," *IEEE Commun. Mag.*, vol. 59, no. 9, pp. 65–71, Sep. 2021.

[17] M. Manzoni et al., "Wavefield networked sensing: Principles, algorithms, and applications," *IEEE Open J. Commun. Soc.*, vol. 6, pp. 181–197, 2025.

[18] F. Liu, Y.-F. Liu, A. Li, C. Masouros, and Y. C. Eldar, "Cramér-Rao bound optimization for joint radar-communication beamforming," *IEEE Trans. Signal Process.*, vol. 70, pp. 240–253, 2021.

[19] F. Zabini, E. Paolini, W. Xu, and A. Giorgetti, "Joint sensing and communications in finite block-length regime," in *Proc. IEEE Global Commun. Conf. (Globecom)*, Rio de Janeiro, Brazil, Dec. 2022, pp. 5595–5600.

[20] F. Zabini, E. Paolini, W. Xu, and A. Giorgetti, "Fundamental limits of cooperative strategies in joint sensing and communication networks," in *Proc. IEEE Int. Conf. Commun. (ICC) Workshops*, Denver, CO, USA, Jun. 2024, pp. 329–334.

[21] C. Giovannetti, N. Decarli, S. Bartoletti, R. A. Stirling-Gallacher, and B. M. Masini, "Target positioning accuracy of V2X sidelink joint communication and sensing," *IEEE Wireless Commun. Lett.*, vol. 13, no. 3, pp. 849–853, Mar. 2024.

[22] L. Pucci, L. Arcangeloni, and A. Giorgetti, "Position and velocity estimation accuracy in MIMO-OFDM ISAC networks: A fisher information analysis," 2025, *arXiv:2507.01743*.

[23] T. Fang, N. T. Nguyen, and M. Juntti, "Low-complexity Cramér-Rao lower bound and sum rate optimization in ISAC systems," in *Proc. IEEE Int. Conf. Acoust. Speech Signal Process. (ICASSP)*, Hyderabad, India, Apr. 2025, pp. 1–5.

[24] H. Hua, J. Xu, and Y. C. Eldar, "Near-field 3D localization via MIMO radar: Cramér-Rao bound analysis and estimator design," *IEEE Trans. Signal Process.*, vol. 72, pp. 3879–3895, Aug. 2024.

[25] X. Li, D. Wang, and X. Ma, "Three-dimensional target localization and Cramér-Rao bound for two-dimensional OFDM-MIMO radar," *Int. J. Antennas Propag.*, vol. 2017, no. 1, Mar. 2017, Art. no. 4171452.

[26] Z. Hu, Q. Ye, Y. Huang, S. Hu, and G. Yang, "Joint range-velocity-azimuth estimation for OFDM-based integrated sensing and communication," *IEEE Trans. Wireless Commun.*, vol. 23, no. 10, pp. 12933–12948, Oct. 2024.

[27] Y. Wang, M. Tao, S. Sun, and W. Cao, "3D extended target sensing in ISAC: Cramér-Rao bound analysis and beamforming design," 2024, *arXiv:2412.06353*.

[28] L. Pucci and A. Giorgetti, "Position error bound for cooperative sensing in MIMO-OFDM networks," in *Proc. IEEE Work. Signal Proc. Adv. Wireless Commun. (SPAWC)*, Lucca, Italy, Sep. 2024, pp. 296–300.

[29] L. Pucci, E. Paolini, and A. Giorgetti, "System-level analysis of joint sensing and communication based on 5G new radio," *IEEE J. Sel. Areas Commun.*, vol. 40, no. 7, pp. 2043–2055, Mar. 2022.

[30] H. L. V. Trees, *Optimum Array Processing: Part IV of Detection, Estimation, and Modulation Theory*.New York, NY, USA: Wiley-Interscience, 2002.
[31] M. A. Richards, *Fundamentals of Radar Signal Processing*.Columbus, OH, USA: McGraw-Hill, 2005.
[32] S. Van de Velde, G. T. F. de Abreu, and H. Steendam, "Improved censoring and NLOS avoidance for wireless localization in dense networks," *IEEE J. Sel. Areas Commun.*, vol. 33, no. 11, pp. 2302–2312, Nov. 2015.
[33] H. Messer, "The hybrid Cramér-Rao lower bound - from practice to theory," in *Proc. IEEE Sens. Array Multichannel Process. Workshop (SAM)*, Waltham, MA, USA, Jul. 2006, pp. 304–307.
[34] Y. Shen and M. Z. Win, "Fundamental limits of wideband localization—Part I: A general framework," *IEEE Trans. Inf. Theory*, vol. 56, no. 10, pp. 4956–4980, Oct. 2010.
[35] Y. Shen, H. Wymeersch, and M. Z. Win, "Fundamental limits of wideband localization—Part II: Cooperative networks," *IEEE Trans. Inf. Theory*, vol. 56, no. 10, pp. 4981–5000, Oct 2010.
[36] S. Van de Velde, G. Abreu, and H. Steendam, "Frame theory and optimal anchor geometries in wireless localization," in *Proc. IEEE Veh. Technol. Conf. (VTC Spring)*, Seoul, South Korea, May 2014, pp. 1–6.
[37] "5G; NR; Physical channels and modulation, (Version 18.2.0, Release 18)," 3GPP, Sophia Antipolis, France, Rep. TS 38.211, May 2024.

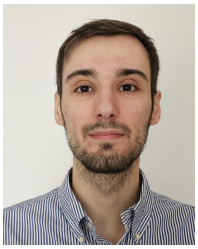

LUCA ARCANGELONI (Member, IEEE) received the M.S. degree (summa cum laude) in electronics and telecommunications engineering from the University of Bologna in 2021, and the Ph.D. degree from the Department of Electrical, Electronic, and Information Engineering, University of Bologna in 2024, where his research focused on spectrum awareness for next-generation wireless networks using statistical methods and machine learning techniques. He is currently a Postdoctoral Researcher with the University of Bologna, working on signal processing techniques for integrated communication and sensing, with a focus on fundamental limits.

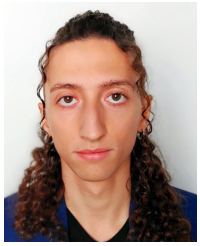

ENRICO TESTI (Member, IEEE) received the M.S. degree (magna cum laude) in electronics and telecommunications engineering for energy and the Ph.D. degree in electronics, telecommunications, and information technologies engineering from the University of Bologna, Italy, in 2018 and 2022, respectively, where he is currently an Assistant Professor with the Department of Electrical, Electronic, and Information Engineering "Guglielmo Marconi." His research interests include artificial intelligence techniques for next-generation wireless networks, massive MIMO, and satellite IoT. He is currently a Secretary/Treasurer of the IEEE ITSoc Italy Section Chapter.

LORENZO PUCCI (Member, IEEE) received the M.S. degree (summa cum laude) in electronics and telecommunications engineering for energy and the Ph.D. degree in electronics, telecommunications, and information technologies engineering from the University of Bologna, Italy, in 2019 and 2024, respectively. In 2023, he was a visiting Ph.D. student with the Technical University of Berlin, Germany. He is currently a Postdoctoral Researcher with the Department of Electrical, Electronic, and Information Engineering, University of Bologna. His research interests include digital communication systems, wireless sensor networks, and integrated sensing and communication.

ANDREA GIORGETTI (Senior Member, IEEE) received the Dr. Ing. degree (summa cum laude) in electronic engineering and the Ph.D. degree in electronic and computer engineering from the University of Bologna, Italy, in 1999 and 2003, respectively.

From 2003 to 2005, he was a Researcher with the National Research Council of Italy. In 2006, he joined the Department of Electrical, Electronic, and Information Engineering "Guglielmo Marconi," University of Bologna, where he is currently an Associate Professor. In Spring 2006, he was a Visiting Researcher with the Laboratory for Information and Decision Systems, Massachusetts Institute of Technology, Cambridge, MA, USA. He is co-author of the book *Cognitive Radio Techniques: Spectrum Sensing, Interference Mitigation, and Localization* (Artech House, 2012). His research interests include integrated sensing and communication, ultra-wideband communication systems, active and passive localization, wireless sensor networks, and cognitive radio.

Dr. Giorgetti has served as a Technical Program Co-Chair for several symposia at the *IEEE International Conference on Communications* and the *IEEE Global Communications Conference*. He has been an Editor of the IEEE COMMUNICATIONS LETTERS and the IEEE TRANSACTIONS ON WIRELESS COMMUNICATIONS. He served as the Chair of the IEEE Communications Society's Radio Communications Technical Committee from 2017 to 2018.